PHYSICAL REVIEW B **92**, 161107(R) (2015)

Prediction of Weyl semimetal in orthorhombic $MoTe_2$

Yan Sun,[1] Shu-Chun Wu,[1] Mazhar N. Ali,[2] Claudia Felser,[1] and Binghai Yan[1,3,4,5,*]

[1]*Max Planck Institute for Chemical Physics of Solids, 01187 Dresden, Germany*

[2]*IBM Almaden Research Center, San Jose, California 95120, USA*

[3]*Max Planck Institute for the Physics of Complex Systems, 01187 Dresden, Germany*

[4]*School of Physical Science and Technology, ShanghaiTech University, Shanghai 200031, China*

[5]*CAS-Shanghai Science Research Center, Shanghai 201203, China*

(Received 4 August 2015; revised manuscript received 28 September 2015; published 9 October 2015)

We investigate the orthorhombic phase (T_d) of the layered transition-metal dichalcogenide $MoTe_2$ as a Weyl semimetal candidate. $MoTe_2$ exhibits four pairs of Weyl points lying slightly above (∼6 meV) the Fermi energy in the bulk band structure. Different from its cousin WTe_2, which was recently predicted to be a type-II Weyl semimetal, the spacing between each pair of Weyl points is found to be as large as 4% of the reciprocal lattice in $MoTe_2$ (six times larger than that of WTe_2). When projected onto the surface, the Weyl points are connected by Fermi arcs, which can be easily accessed by angle-resolved photoemission spectroscopy due to the large Weyl point separation. In addition, we show that the correlation effect or strain can drive $MoTe_2$ from a type-II to a type-I Weyl semimetal.

DOI: 10.1103/PhysRevB.92.161107 PACS number(s): 73.20.At, 71.20.−b

I. INTRODUCTION

The Weyl semimetal (WSM) is a topological semimetal [1–3] in which bands disperse linearly in three-dimensional (3D) momentum space through a node, called a Weyl point (WP). The WP acts as a monopole with fixed chirality [4], a source or a sink of the Berry curvature. Similar to those of a topological insulator (TI), topologically protected surface states exist on the surface of a WSM. Topologically different from ordinary Fermi surfaces (FSs), these surface states present unclosed FSs, called Fermi arcs, which connect the surface projections of WPs with opposite chirality [2]. WSMs also exhibit exotic quantum transport phenomena, such as the chiral anomaly [5–7] characterized by negative longitudinal magnetoresistance (MR) [8], an anomalous Hall effect [3,9–11], and nonlocal transport properties [12,13].

Recently, the first WSM materials (Ta,Nb)(As,P) have been discovered by addressing the Fermi arcs in angle-resolved photoemission spectra (ARPES) [14–20], which were originally predicted by band structure calculations [21,22]. Meanwhile, a great amount of effort has also been devoted to their magnetotransport properties [23–29], such as extremely large, positive transverse MR [23] and large, negative longitudinal MR [24,29]. This family of WSMs exhibits ideal Weyl cones in the bulk band structure, i.e., the FS shrinks into a point at the WP. Very recently, Soluyanov *et al.* proposed a new type of WSM in the compound WTe_2 [30], referred to as type-II WSM [31]. Herein, the Weyl cone is strongly tilted so that the WP exists at the touching point of the electron and hole pockets in the FS, which may indicate a salient response to the magnetic field. Topological Fermi arcs were demonstrated between a pair of WPs that are separated by ∼0.7% of the reciprocal lattice vector length and lie about 50 meV above the Fermi energy (E_F).

Provoked by WTe_2 [31], we predict that the orthorhombic phase of $MoTe_2$, which was synthesized very recently [32], is a different type-II WSM candidate. The layered transition-metal dichalcogenide $MoTe_2$ can crystalize into three phases in different experimental conditions: the $2H$, $1T'$, and T_d phases. The $2H$ phase is semiconducting, in which the Mo atom has trigonal prismatic coordination with the Te atoms. The $1T'$ (also called the β phase) [33] and T_d phases are semimetallic and exhibit pseudohexagonal layers with zigzag metal chains. The $1T'$ phase is a monoclinic lattice that is stable at room temperature, arising from the slight sliding of layer stacking of the orthorhombic lattice of the T_d phase [see Fig. 1(a)]. The T_d compound can be obtained by cooling the $1T'$ phase down to 240 K [32,34,35]. We note that the $1T'$ structure exhibits inversion symmetry (space group $P12_1/m1$, No. 11) while the T_d one does not (space group $Pmn2_1$, No. 31). The $1T'$ phase of $MoTe_2$ was speculated to be a WSM candidate as pressurized WTe_2 in Ref. [31]. We note that, however, the $1T'$ phase cannot be a WSM simply because of the coexistence of time-reversal symmetry (TRS) and inversion symmetry, because the WSM requires the breaking of at least one of the TRSs and inversion symmetry. Therefore, only the T_d phase, which is isostructural to WTe_2, can be a possible WSM.

In this Rapid Communication, we investigate the T_d-$MoTe_2$ as a WSM candidate by *ab initio* density-functional theory (DFT) calculations. We indeed find four pairs of WPs in the band structure [see Fig. 1(c)], similar to WTe_2. Each pair of WPs exhibits considerable spacing in the Brillouin zone, ∼4.2% of the reciprocal lattice vector, in which one WP exists merely 6 meV above E_F and the other WP lies 59 meV above E_F. We observe clear Fermi arcs in the surface state calculations. Due to the large momentum spacing and the close vicinity to E_F of the WPs, we expect that the Fermi arcs and other interesting quantum phenomena of $MoTe_2$ will be easily accessed by future ARPES and transport experiments.

II. METHODS AND CRYSTAL STRUCTURE

DFT calculations were performed with the Vienna *ab initio* simulation package (VASP) [36] with a projected augmented wave (PAW) potential. The exchange and correlation energy

*yan@cpfs.mpg.de

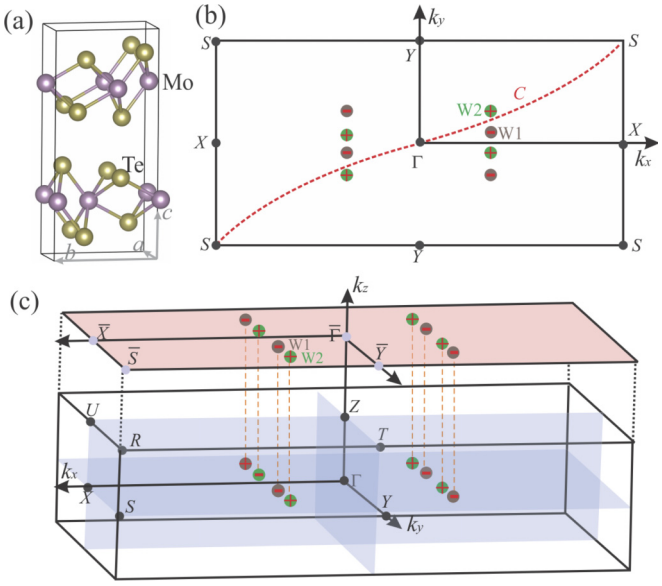

FIG. 1. (Color online) (a) Orthorhombic crystal lattice structure of T_d-$MoTe_2$ in the space group of $Pnm2_1$. (b) Brillouin zone (BZ) in the $k_z = 0$ plane. WPs with positive and negative chiralities are marked as green and gray dots. The evolution of Wannier charge centers between the Γ and S points is calculated along the red curve C. (c) 3D bulk BZ and the projected surface BZ to the (001) plane.

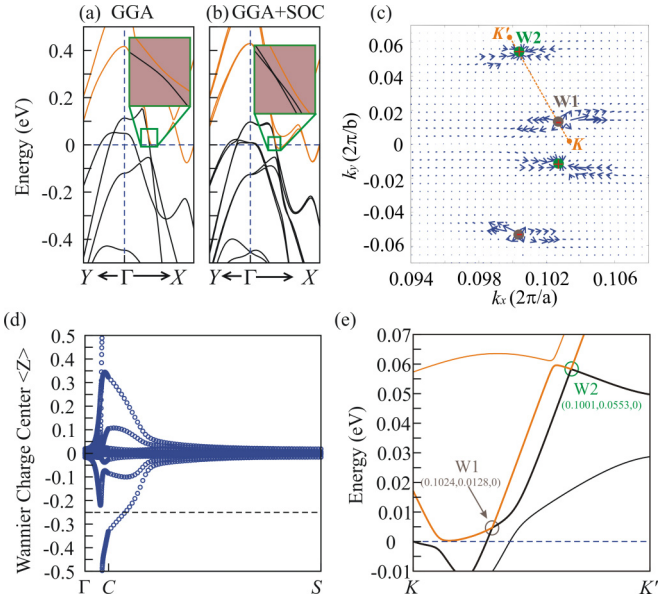

FIG. 2. (Color online) Bulk band structure around the Γ point in the Y-Γ-X direction (a) without and (b) with the inclusion of SOC. (c) Berry curvature in the $k_z = 0$ plane around two types of WPs. The sizes and directions of the arrows represent the magnitudes and orientations of the Berry curvature, respectively. WPs with positive and negative chirality are denoted by the green and gray points. (c) The evolution of Wannier charge centers between two time-reversal-invariant points of Γ and S along the C curve [see Fig. 1(b)]. The Wannier charge centers cross the reference horizontal line once, indicating the nontrivial Z_2 invariant in the C-k_z plane. (e) Band structure crossing two types of WPs. The two points of K and K' are shown in (c). Black and orange bands in (a), (b), and (e) are the lowest Nth bands and other higher bands, respectively.

was considered in both the generalized gradient approximation (GGA) [37] level with a Perdew-Burke-Ernzerhof (PBE) functional and a hybrid functional (HSE06) [38]. The energy cutoff was set to 300 eV for a plane wave basis. The tight-binding matrix was constructed by projecting the Bloch states into maximally localized Wannier functions (MLWFs) [39]. We employed the experimental lattice parameters and atomic positions measured by our recent experiment [32]. For completeness, the lattice constants are $a = 3.477$ Å, $b = 6.335$ Å, and $c = 13.883$ Å. There are four Mo atoms and eight Te atoms in the primitive unit cell. All the atoms are located at the $2a$ sites of the $Pmn2_1$ space group with reduced positions of Mo: (0.0, 0.605 20, 0.500 34), (0.0, 0.030 10, 0.014 74); and Te: (0.0, 0.862 57, 0.655 74), (0.0, 0.640 45, 0.112 46), (0.0, 0.289 97, 0.859 34), and (0.0, 0.216 01, 0.402 72).

III. RESULTS AND DISCUSSIONS

The T_d-$MoTe_2$ exhibits a semimetallic feature in the band structure, as shown in Figs. 2(a) and 2(b). We refer to the lowest Nth bands (black bands) as the valence bands of a semimetal and the other higher bands (orange bands) as the conduction bands at each k point, where N is the number of total valence electrons. When spin-orbital coupling (SOC) is taken into consideration, the spin degeneracy is lifted up in the band structure due to the lack of inversion symmetry. A tiny direct gap between the conduction and valence bands exists at the one fifth position of the Γ-X line. However, near this point a pair of linearly band-crossing points exists aside from the high symmetry Γ-X line, as shown in Fig. 2(e). One point is merely 6 meV above E_F (labeled as W1) and the other is 59 meV above E_F (labeled as W2).

To validate the topology of W1 and W2 band-crossing points, we investigate the Berry curvature in the $k_z = 0$ plane calculated from the tight-binding Hamiltonian with MLWFs. The Berry curvature is integrated over all the N valence bands, by assuming a k-dependent chemical potential between the Nth and $(N + 1)$th bands at each k point of the BZ. In Fig. 2(c), one can clearly find two monopoles, W2 as a source and W1 as a sink of the Berry curvature in the positive part of the BZ. It directly confirms that W1 and W2 are a pair of WPs with opposite chirality. By tracing the monopole centers of Berry curvatures, we found that the coordinates of the two WPs are W1-$(0.1024\frac{2\pi}{a}, 0.0128\frac{2\pi}{b}, 0)$ and W2-$(0.1001\frac{2\pi}{a}, 0.0530\frac{2\pi}{b}, 0)$, respectively, which is consistent with the band structure of Fig. 2(e). Considering the existence of mirror symmetry in the xz (glide plane) and yz planes, four pairs of WPs in total can be found in the BZ [Fig. 1(c)].

The existence of TRS allows us to define a Z_2 topological invariant [40] on a surface with a direct energy gap. We choose a contour C that connects the S, Γ, and $-S$ points by crossing pairs of WPs and that respects the TRS [see Fig. 1(b)]. Since only WPs in the $k_z = 0$ plane are gapless, the C-k_z surface is gapped everywhere. Thus, we can compute the Z_2 invariant by tracing the Wannier charge centers projected to the z axis ($\langle Z \rangle$) using the non-Abelian Berry connection [41,42]. The time-reversal partners exhibit a clear switch between the

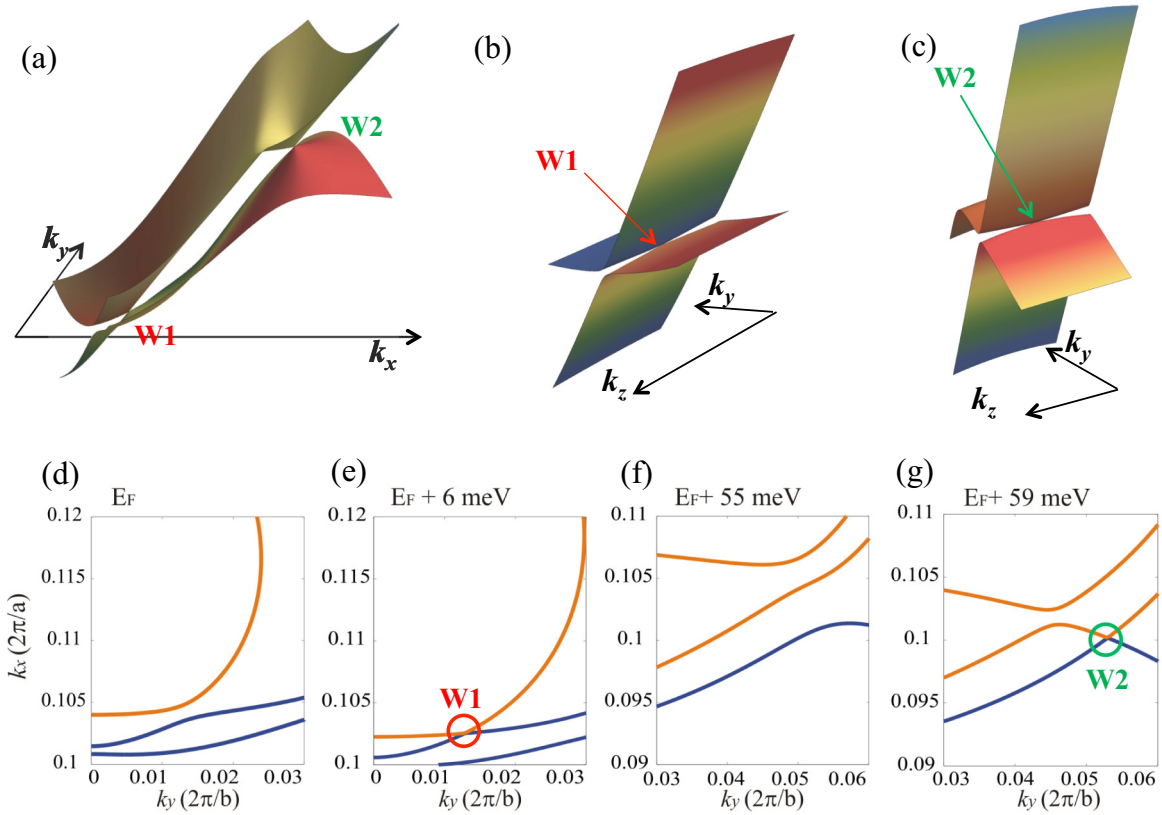

FIG. 3. (Color online) 3D plot of WPs in (a) $k_z = 0$, (b) $k_x = 0.1024\frac{2\pi}{a}$, and (c) $k_x = 0.1001\frac{2\pi}{a}$ planes. (d)–(g) The evolution of FS around two WPs in the $k_z = 0$ plane. WP-related Fermi surface linear crossings can be at $E_F + 6$ meV and $E_F + 59$ meV, respectively. The orange and blue FSs come from the electron and hole pockets.

Γ and S points along the contour C during time-reversal pumping [43]. The nontrivial Z_2 index is characterized by the odd number of times the Wannier centers cross through the horizontal reference line in Fig. 2(d). It protects the existence of helical edge states along the C projection to the surface BZ, which form part of the Fermi arcs between WPs with opposite chirality, if the k_z direction is cut to an open surface.

We note that the distance between W1 and W2 WPs is 4.2% of the reciprocal lattice, which is almost six times larger than that in WTe_2 [31]. Therefore, the Fermi arcs connecting W1 and W2 should be much easier to measure by ARPES in $MoTe_2$ than in WTe_2. Compared to that of WTe_2, the valence and conduction bands locate even closer to each other along the Γ-X line, which may be attributed to the structural differences between WTe_2 and $MoTe_2$. As a consequence, pairs of WPs are separated more in $MoTe_2$ than in WTe_2. Given that W1 is 6 meV above E_F, only a small amount of doping is required to shift the chemical potential to the WPs.

We show the 3D energy dispersion of the Weyl cones in Fig. 3. Linear dispersions exist along all momentum directions through the nodes of the W1 and W2 points. Because of the weak van der Waals interactions in the z direction, the Fermi velocity is much smaller in the k_z direction than that in the k_x-k_y plane. Figures 3(d)–3(g) show the evolution of FSs in the $k_z = 0$ plane. At E_F, the electron (orange curves) and hole (blue curves) pockets are separated by a gap. When the energy increases, the electron and hole pockets extend and and shrink, respectively. At $E_F + 6$ meV, electron and hole pockets touch each other at the W1 point, as shown in Fig. 3(e). When further increasing the energy, a new gap opens at the W1 touching point until the second electron hole touches the appeasers at the W2 point at $E_F + 59$ meV in Fig. 3(f). We can clearly see that W1 and W2 WPs in $MoTe_2$ are formed by the touching points between the electron and hole pockets in the FS, which is exactly the type-II WSM proposed in Ref. [31]. Therefore, one can also expect the appearance of Fermi arcs when the E_F crosses the WPs.

Next, we examine the Fermi arcs on the (001) surface. We consider a half-infinite surface using the iterative Green's function method [44,45]. The k-dependent local density of states (LDOS) are projected from the half-infinite bulk to the outermost surface unit cell to demonstrate the surface band structure. Except for a small electron pocket near the $\overline{Y}$ point, the FSs mainly distribute in the center region of the surface BZ. So we will focus on this region that includes all surface projections of WPs.

One can see large electron and hole pockets in the FS of Fig. 4(a). The hole pockets appear near the $\overline{\Gamma}$ point and the electron pockets exist in the middle of $\overline{\Gamma}-\overline{X}$, which is consistent with the bulk band structure. As presented in Figs. 4(b) and 4(c), $E_F + 6$ meV, a Fermi arc starts from the W1 point and ends at the position near the W2 point. Meanwhile, a trivial FS coexists, which is a closed circle with a part merging into the bulk electron pocket. We illustrate these FSs in Fig. 4(d) for a simple understanding of the surface states. Because the W1 and W2 WPs do not lie at

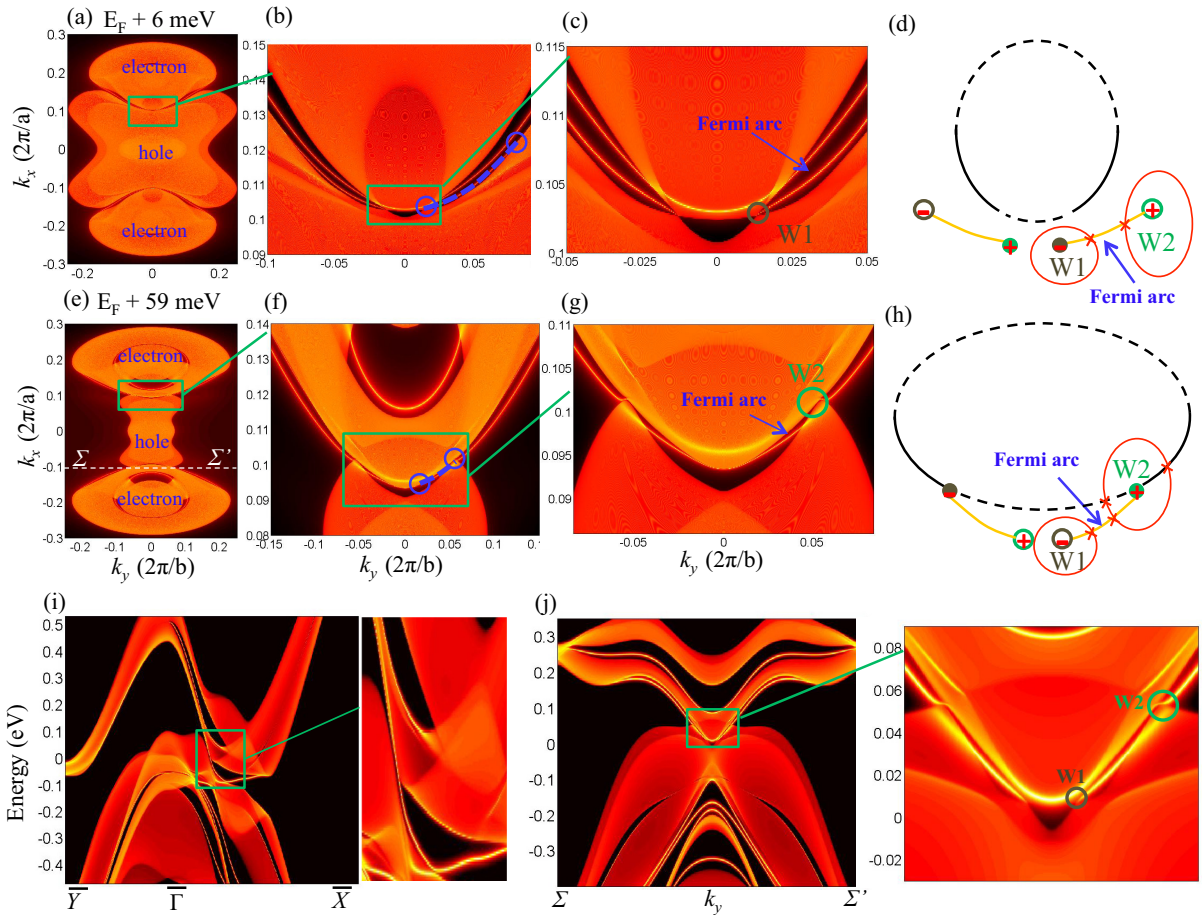

FIG. 4. (Color online) Fermi surfaces and surface band structures. (a)–(c) Surface FS and (d) the illustration of Fermi arcs at $E_F + 6$ meV. (f), (g) Surface FSs and (h) corresponding schematics at $E_F + 59$ meV. (i) Surface energy dispersion along the high symmetry lines of $\overline{Y}$-$\overline{\Gamma}$-$\overline{X}$. (j) Surface energy dispersion along the Σ-Σ' crossing WPs. Brighter colors represent the higher LDOS. The exact projections of W1 and W2 are denoted as solid gray and green dots. The end points of Fermi arcs are marked as open circles. The Fermi arcs are highlighted by dashed lines in (b) and (f).

the same energy, the end point of the Fermi arc cannot exactly be the surface projection of W2. As shown in Fig. 4(c), the starting point is the W1 projection, while the other end point is $(0.1215\frac{2\pi}{a}, 0.0805\frac{2\pi}{b})$, relatively far away from the W2 projection, just as expected. As a consequence, the length of the surface Fermi arc at $E_F + 6$ meV is much larger than the separation of W1 and W2 points in the bulk, ~7% of the reciprocal lattice, which provides an advantage for ARPES detection. When shifting E_F to the W2 position, the electron pockets expand and the hole pockets shrink, and the Fermi arcs remain in the surface BZ. At $E_F + 59$ meV, the end point of the Fermi arc becomes exactly the projection of the W2 point, while the starting point shifts to $(0.0931\frac{2\pi}{a}, 0.0040\frac{2\pi}{b})$, which is close to the W1 projection. Here, the Fermi arc is as long as ~5% of the reciprocal lattice. We note that the trivial Fermi circle now merges into the W2 point, as illustrated in Fig. 4(h), but this does not change the topology of the FS.

We can understand further the Fermi arc states from the band structure with energy resolution. In Fig. 4(i) we can see several surface states disperse at the boundary of conduction bands and the valence bands along $\overline{\Gamma}$-$\overline{X}$, But their FSs are just closed circles, e.g., those in Figs. 4(d) and 4(h). Since the line connecting W1-W2 is almost parallel to the k_y axis, we plot the band structure along the k_y line Σ-Σ' [indicated in Fig. 4(e)]. As shown in Fig. 4(j), a surface band connects to W1 and W2 in the range of ~5 to ~55 meV above the Fermi level, which is consistent with the bulk band structure. This state forms the Fermi arc observed in the FS.

We should point out that the band structure of $MoTe_2$ is very sensitive to structural distortion. For example, a small strain of 1% can annihilate two pairs of W1 WPs and leave only W2 WPs. Moreover, the W2 WPs turn from type II to normal type I as a touching point by the valence band top and the conduction band bottom, as illustrated in Fig. 5(c). Considering that GGA often underestimates the correlation effect and overestimates the band inversion, we further performed band structure calculations using the hybrid-functional method (HSE06) [38]. From the hybrid-functional calculations, we find that the original W1 WPs disappear and W2 WPs change into type I. New WPs lie 45 meV above the Fermi level, as the band structure showing in Fig. 5(a). In the surface band structures [Fig. 5(b)], the topological surface band connects a pair of WPs with opposite chirality, which relates to the Fermi arc. As presented in Figs. 5(d) and 5(e), at the energy $E = E_F + 45$ meV there is one Fermi curve starting from the WP in the positive zone of the two-dimensional (2D)

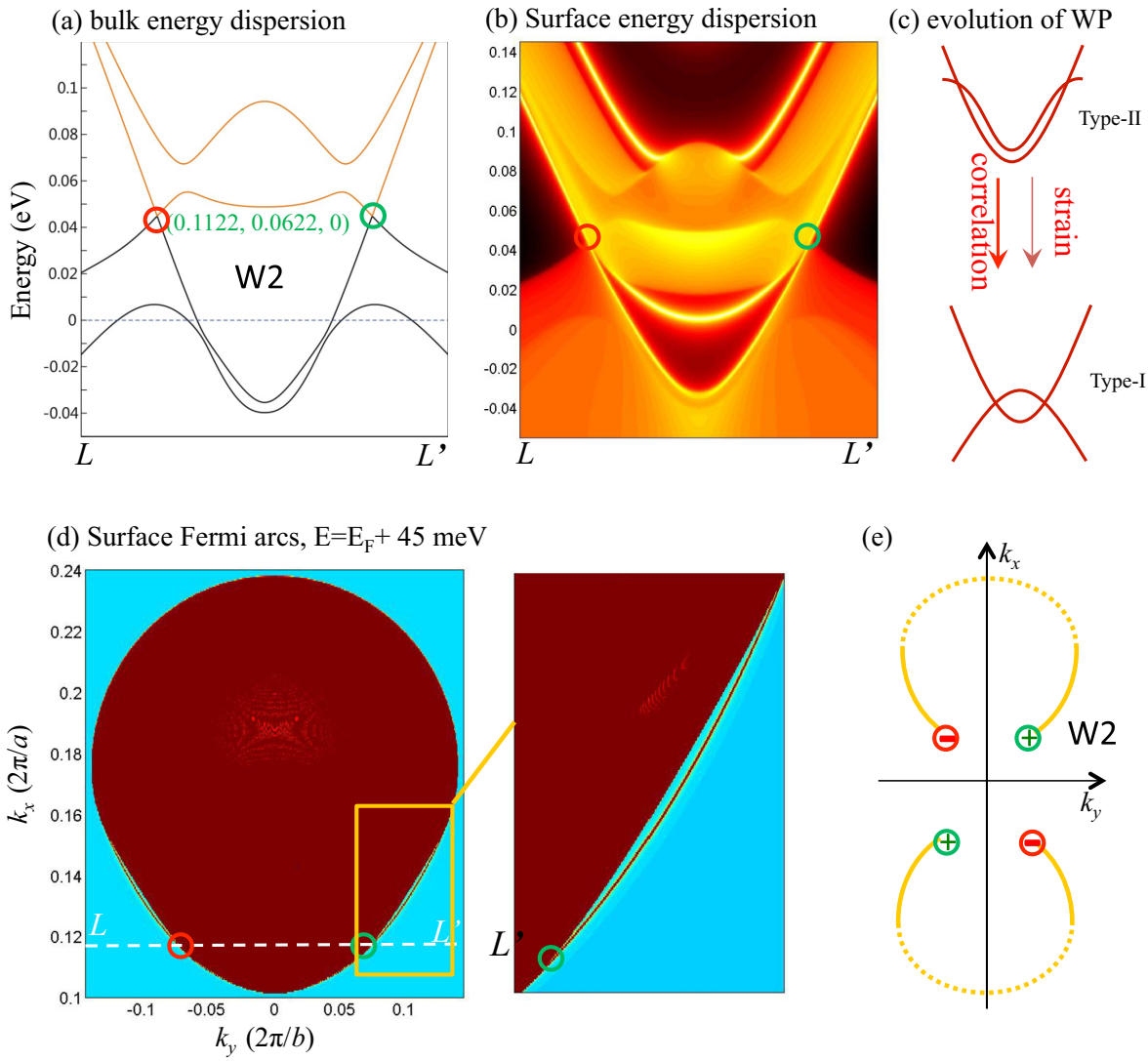

FIG. 5. (Color online) Electronic structure calculated from the hybrid functional. (a) Bulk band structure along two WPs in the k_y directions, and (b) corresponding surface energy dispersion. (c) Schematic of WP evolution with correlation and compression strain. (d) Surface FS at the energy level of $E = E_F + 45$ meV and (e) corresponding schematics for the surface Fermi arcs. The two points of L and L' are shown in (d). The red and green circles represent WPs with opposite chirality.

BZ and submerging into the bulk state around the point of $(0.155\frac{2\pi}{a}, 0.125\frac{2\pi}{b})$. This Fermi curve extends out on the left side of the bulk state and finally ends at the other WP with opposite chirality. This curve is the Fermi arc that connects a pair of WPs with opposite chirality. Figure 5(c) illustrates the transition from type-II to type-I WSMs due to the strain or the correlation effect. Such a phase transition should be considered when interpreting future experiments, due to the uncertainty of the realistic correlation effect and the lack of knowledge about lattice contraction at low temperatures.

IV. SUMMARY

In summary, we find the WSM state and reveal the topological Fermi arcs in orthorhombic $MoTe_2$. By *ab initio* calculations we observe four pairs of WPs with opposite chirality lying on the $k_z = 0$ plane of the BZ. One type of WP is just 6 meV above the E_F, and the other is at $E_F + 59$ meV, which can be accessed by slight electron doping. The spacing between WP pairs is as long as 4.2% of the reciprocal lattice, six times larger than that of WTe_2. Connecting the surface projections of WPs, topological Fermi arcs exist, which calls for an experimental verification such as by ARPES. The correlation effect or strain is expected to induce transitions from type-II to type-I WSMs in $MoTe_2$, which calls for experimental verification.

ACKNOWLEDGMENTS

We are grateful to Y. P Qi and B. A. Bernevig for helpful discussions. This work was financially supported by the Deutsche Forschungsgemeinschaft DFG (Project No. EB 518/1-1 of DFG-SPP 1666 "Topological Insulators," and SFB 1143) and by the ERC (Advanced Grant No. 291472 "Idea Heusler").

[1] G. E. Volovik, in *Quantum Analogues: From Phase Transitions to Black Holes and Cosmology*, edited by W. G. Unruh and R. Schutzhold, Springer Lecture Notes in Physics Vol. 718 (Springer, Berlin, 2007), pp. 31–73.

[2] X. G. Wan, A. M. Turner, A. Vishwanath, and S. Y. Savrasov, Topological semimetal and Fermi-arc surface states in the electronic structure of pyrochlore iridates, Phys. Rev. B **83**, 205101 (2011).

[3] A. A. Burkov and L. Balents, Weyl Semimetal in a Topological Insulator Multilayer, Phys. Rev. Lett. **107**, 127205 (2011).

[4] H. B. Nielsen and M. Ninomiya, Absence of neutrinos on a lattice: (I). Proof by homotopy theory, Nucl. Phys. B **185**, 20 (1981).

[5] S. L. Adler, Axial-vector vertex in spinor electrodynamics, Phys. Rev. **177**, 2426 (1969).

[6] J. S. Bell and R. Jackiw, A PCAC puzzle: $\pi^0 \to \gamma\gamma$ in the σ-model, Nuovo Cimento A **60**, 47 (1969).

[7] R. A. Bertlmann, *Anomalies in Quantum Field Theory*, Vol. 91 (Oxford University Press, Oxford, UK, 2000).

[8] H. B. Nielsen and M. Ninomiya, The Adler-Bell-Jackiw anomaly and Weyl fermions in a crystal, Phys. Lett. B **130**, 389 (1983).

[9] G. Xu, H. Weng, Z. Wang, X. Dai, and Z. Fang, Chern Semimetal and the Quantized Anomalous Hall Effect in $HgCr_2Se_4$, Phys. Rev. Lett. **107**, 186806 (2011).

[10] K.-Y. Yang, Y.-M. Lu, and Y. Ran, Quantum Hall effects in a Weyl semimetal: Possible application in pyrochlore iridates, Phys. Rev. B **84**, 075129 (2011).

[11] A. G. Grushin, Consequences of a Condensed Matter Realization of Lorentz-Violating QED in Weyl Semimetals, Phys. Rev. D **86**, 045001 (2012).

[12] S. A. Parameswaran, T. Grover, D. A. Abanin, D. A. Pesin, and A. Vishwanath, Probing the Chiral Anomaly with Nonlocal Transport in Three-Dimensional Topological Semimetals, Phys. Rev. X **4**, 031035 (2014).

[13] C. Zhang, E. Zhang, Y. Liu, Z.-g. Chen, S. Liang, J. Cao, X. Yuan, L. Tang, Q. Li, T. Gu, Y. Wu, J. Zou, and F. Xiu, Detection of chiral anomaly and valley transport in Dirac semimetals, arXiv:1504.07698.

[14] S.-Y. Xu, I. Belopolski, N. Alidoust, M. Neupane, G. Bian, C. Zhang, R. Sankar, G. Chang, Z. Yuan, C.-C. Lee, S.-M. Huang, H. Zheng, J. Ma, D. S. Sanchez, B. Wang, A. Bansil, F. Chou, P. P. Shibayev, H. Lin, S. Jia, and M. Z. Hasan, Discovery of a Weyl fermion semimetal and topological Fermi arcs, Science **349**, 613 (2015).

[15] B. Q. Lv, H. M. Weng, B. B. Fu, X. P. Wang, H. Miao, J. Ma, P. Richard, X. C. Huang, L. X. Zhao, G. F. Chen, Z. Fang, X. Dai, T. Qian, and H. Ding, Experimental Discovery of Weyl Semimetal TaAs, Phys. Rev. X **5**, 031013 (2015).

[16] L. X. Yang, Z. K. Liu, Y. Sun, H. Peng, H. F. Yang, T. Zhang, B. Zhou, Y. Zhang, Y. F. Guo, M. Rahn, D. Prabhakaran, Z. Hussain, S.-K. Mo, C. Felser, B. Yan, and Y. L. Chen, Weyl semimetal phase in the non-centrosymmetric compound TaAs, Nat. Phys. **11**, 728 (2015).

[17] B. Q. Lv, N. Xu, H. M. Weng, J. Z. Ma, P. Richard, X. C. Huang, L. X. Zhao, G. F. Chen, C. Matt, F. Bisti, V. Strokov, J. Mesot, Z. Fang, X. Dai, T Qian, M. Shi, and H. Ding, Observation of Weyl nodes in TaAs, Nat. Phys. **11**, 724 (2015).

[18] Z. K. Liu, L. X. Yang, Y. Sun, T. Zhang, H. Peng, H. F. Yang, C. Chen, Y. Zhang, Y. F. Guo, P. Dharmalingam, M. Schmidt, Z. Hussain, S. K. Mo, C. Felser, B. Yan, and Y. L. Chen (unpublished).

[19] S.-Y. Xu, N. Alidoust, I. Belopolski, Z. Yuan, G. Bian, T.-R. Chang, H. Zheng, V. N. Strocov, D. S. Sanchez, G. Chang, C. Zhang, D. Mou, Y. Wu, L. Huang, C.-C. Lee, S.-M. Huang, B. Wang, A. Bansil, H.-T. Jeng, T. Neupert, A. Kaminski, H. Lin, S. Jia, and M. Z. Hasan, Discovery of a Weyl fermion state with Fermi arcs in niobium arsenide, Nat. Phys. **11**, 748 (2015).

[20] N. Xu, H. M. Weng, B. Q. Lv, C. Matt, J. Park, F. Bisti, V. N. Strocov, D. Gawryluk, E. Pomjakushina, K. Conder, N. C. Plumb, M. Radovic, G. Autès, O. V. Yazyev, Z. Fang, X. Dai, G. Aeppli, T. Qian, J. Mesot, H. Ding, and M. Shi, Observation of Weyl nodes and Fermi arcs in TaP, arXiv:1507.03983.

[21] H. Weng, C. Fang, Z. Fang, B. A. Bernevig, and X. Dai, Weyl Semimetal Phase in Noncentrosymmetric Transition-Metal Monophosphides, Phys. Rev. X **5**, 011029 (2015).

[22] S.-M. Huang, S.-Y. Xu, I. Belopolski, C.-C. Lee, G. Chang, B. Wang, N. Alidoust, G. Bian, M. Neupane, C. Zhang, S. Jia, A. Bansil, H. Lin, and M. Z. Hasan, A Weyl Fermion semimetal with surface Fermi arcs in the transition metal monopnictide TaAs class, Nat. Commun. **6**, 7373 (2015).

[23] C. Shekhar, A. K. Nayak, Y. Sun, M. Schmidt, M. Nicklas, I. Leermakers, U. Zeitler, Y. Skourski, J. Wosnitza, Z. Liu, Y. Chen, W. Schnelle, H. Borrmann, Y. Grin, C. Felser, and B. Yan, Extremely large magnetoresistance and ultrahigh mobility in the topological Weyl semimetal candidate NbP, Nat. Phys. **11**, 645 (2015).

[24] C. Shekhar, F. Arnold, S.-C. Wu, Y. Sun, M. Schmidt, N. Kumar, A. G. Grushin, J. H. Bardarson, R. Donizeth dos Reis, M. Naumann, M. Baenitz, H. Borrmann, M. Nicklas, E. Hassinger, C. Felser, and B. Yan, Large and unsaturated negative magnetoresistance induced by the chiral anomaly in the Weyl semimetal TaP, arXiv:1506.06577.

[25] X. Huang, L. Zhao, Y. Long, P. Wang, D. Chen, Z. Yang, H. Liang, M. Xue, H. Weng, Z. Fang, X. Dai, and G. Chen, Observation of the Chiral Anomaly Induced Negative Magnetoresistance in 3D Weyl Semimetal TaAs, Phys. Rev. X **5**, 031023 (2015).

[26] C. Zhang, S.-Y. Xu, I. Belopolski, Z. Yuan, Z. Lin, B. Tong, N. Alidoust, C.-C. Lee, S.-M. Huang, H. Lin, M. Neupane, D. S. Sanchez, H. Zheng, G. Bian, J. Wang, C. Zhang, T. Neupert, M. Z. Hasan, and S. Jia, Observation of the Adler-Bell-Jackiw chiral anomaly in a Weyl semimetal, arXiv:1503.02630.

[27] Z. Wang, Y. Zheng, Z. Shen, Y. Zhou, X. Yang, Y. Li, C. Feng, and Z.-A. Xu, Helicity protected ultrahigh mobility Weyl fermions in NbP, arXiv:1506.00924.

[28] X. Yang, Y. Liu, Z. Wang, Y. Zheng, and Z.-A. Xu, Chiral anomaly induced negative magnetoresistance in topological Weyl semimetal NbAs, arXiv:1506.03190.

[29] J. Du, H. Wang, Q. Mao, R. Khan, B. Xu, Y. Zhou, Y. Zhang, J. Yang, B. Chen, C. Feng, and M. Fang, Unsaturated both large positive and negative magnetoresistance in Weyl Semimetal TaP, arXiv:1507.05246.

[30] M. N. Ali, J. Xiong, S. Flynn, J. Tao, Q. D. Gibson, L. M. choop, T. Liang, N. Haldolaarachchige, M. Hirschberger, N. P. Ong, and R. J. Cava, Large, non-saturating magnetoresistance in WTe_2, Nature **514**, 205 (2014).

[31] A. A. Soluyanov, D. Gresch, Z. Wang, Q. Wu, M. Troyer, X. Dai, and B. A. Bernevig, A new type of Weyl semimetal, arXiv:1507.01603.

[32] Y. Qi, P. G. Naumov, M. N. Ali, C. R. Rajamathi, Y. Sun, C. Shekhar, S.-C. Wu, V. Suß, M. Schmidt, E. Pippel, P. Werner, R. Hillebrand, T. Forster, E. Kampertt, W. Schnelle, S. Parkin, R. J. Cava, C. Felser, B. Yan, and S. A. Medvedev, Superconductivity in the Weyl semimetal candidate $MoTe_2$, arXiv:1508.03502.

[33] B. E. Brown, The crystal structures of WTe_2 and high-temperature $MoTe_2$, Acta Crystallogr. **20**, 268 (1966).

[34] H. P. Hughes and R. H. Friend, Electrical resistivity anomaly in β-$MoTe_2$ (metallic behavior), J. Phys. C: Solid State Phys. **11**, L103 (1978).

[35] T. Zandt, H. Dwelk, C. Janowitz, and R. Manzke, Quadratic temperature dependence up to 50 K of the resistivity of metallic $MoTe_2$, J. Alloys Compd. **442**, 216 (2007).

[36] G. Kresse and J. Furthmüller, Efficient iterative schemes for *ab initio* total-energy calculations using a plane-wave basis set, Phys. Rev. B **54**, 11169 (1996).

[37] J. P. Perdew, K. Burke, and M. Ernzerhof, Generalized Gradient Approximation Made Simple, Phys. Rev. Lett. **77**, 3865 (1996).

[38] J. Heyd, G. E. Scuseria, and M. Ernzerhof, Hybrid functionals based on a screened Coulomb potential, J. Chem. Phys. **118**, 8207 (2003).

[39] A. A. Mostofi, J. R. Yates, Y.-S. Lee, I. Souza, D. Vanderbilt, and N. Marzari, Wannier90: A tool for obtaining maximally-localised Wannier functions, Comput. Phys. Commun. **178**, 685 (2008).

[40] C. L. Kane and E. J. Mele, Z_2 Topological Order and the Quantum Spin Hall Effect, Phys. Rev. Lett. **95**, 146802 (2005).

[41] A. A. Soluyanov and D. Vanderbilt, Computing topological invariants without inversion symmetry, Phys. Rev. B **83**, 235401 (2011).

[42] R. Yu, X. L. Qi, B. A. Bernevig, Z. Fang, and X. Dai, Equivalent expression of $\mathbb{Z}_2$ topological invariant for band insulators using the non-Abelian Berry connection, Phys. Rev. B **84**, 075119 (2011).

[43] L. Fu and C. L. Kane, Time reversal polarization and a Z_2 adiabatic spin pump, Phys. Rev. B **74**, 195312 (2006).

[44] M. P. Lopez Sancho, J. M. Lopez Sancho, and J. Rubio, Quick iterative scheme for the calculation of transfer matrices: Application to Mo (100), J. Phys. F: Met. Phys. **14**, 1205 (1984).

[45] M. P. Lopez Sancho, J. M. Lopez Sancho, and J. Rubio, Highly convergent schemes for the calculation of bulk and surface Green functions, J. Phys. F: Met. Phys. **15**, 851 (1985).